


PAPER



Cite this: *Soft Matter*, 2018, 14, 5080

Simulation of the optimal diameter and wall thickness of hollow Fe₃O₄ microspheres in magnetorheological fluids†

Lei Pei, Haoming Pang, Kaihui Chen, Shouhu Xuan* and Xinglong Gong *

This work reported a simulation study on the optimal diameter (D) and wall thickness (H) of hollow Fe₃O₄ microspheres to improve the magnetorheological (MR) effect. Modified formulae for the magnetic dipolar force, van der Waals force, and hydrodynamic drag force were employed in the simulation model. Typical evolution of shear stress and microstructures in steady shear flow was obtained. The shear stress–strain curve was divided into linear, fluctuant, and homeostasis regions, which were related to the inclination of particle chains and the lateral aggregation. For hollow Fe₃O₄ microspheres with different diameters and wall thicknesses, the shear stress curves collapsed onto a quadratic master curve. The best wall thickness was $H = 0.39D$ for a 20 wt% MR fluid and $H = 0.35D$ for a 40 wt% MR fluid, while the optimal diameter was $D = 1000$ nm and $D = 100$ nm, respectively. The maximum shear stress of the 40 wt% MR fluid was twice that of the 20 wt% MR fluid. The change of shear stress was due to the competition that results among the magnetic interaction, number of neighbors, tightness, and orientation of the particle chains. Simulated dimensionless viscosity data as a function of Mason number for various diameters, wall thicknesses, and weight fractions collapsed onto a single master curve. The simulated shear stress under both a magnetic field and shear rate sweep matched well with experiments.

Received 5th April 2018,
Accepted 25th May 2018

DOI: 10.1039/c8sm00704g

rsc.li/soft-matter-journal

Introduction

Magnetorheological (MR) fluid is a two-phase system consisting of well dispersed magnetic particles and a nonmagnetic matrix.¹ Due to the magnetic dipolar forces, the viscosity and yield stress of this smart material could increase several orders of magnitude in milliseconds. The reversible and controllable MR effect means that MR fluid is widely applied in magnetic-thermal therapy, drug targeting delivery, commercial dampers, and sensors *etc.*^{2–7} Fe₃O₄ micro or nanoparticles are commonly used in conventional MR fluids as a consequence of their high saturation magnetization, super-paramagnetic property, and common availability. Raising the MR effect and overcoming the sediment problem are the main challenges for the Fe₃O₄-based MR fluid. The former is related to the weight fraction, magnetic permeability, shape and morphology of the magnetic particles.^{8–10} It is reported that a flaky and fibrous particle-based MR fluid exhibited excellent MR effects.^{11,12} However, the aforementioned particles cannot overcome the inherent sedimentation due to the density mismatch with the matrix.

The sediment problem is usually reduced through bi-dispersing and surface coating methods.^{13,14} The stabilization mechanisms of suspensions containing octane droplets and particles modified with short amphiphiles were investigated.¹⁵ Emulsion stabilization could be achieved through a compact layer of particles around the oil droplet or a percolating network of particles spanning throughout the continuous phase. Improving the inner particle architecture is a novel approach to overcome sedimentation, which has attracted researchers' interests in the past few decades. A core-shell and hollow architecture can enlarge the MR effect and decrease the particle density at the same time.^{16,17} Magnetic materials are often immobilized onto the surface of the non-magnetic template to form core-shell particles, such as CNT@Fe₃O₄ and PS@Fe₃O₄ microspheres.^{18,19} Hollow spheres possess a larger specific surface area and larger weight fraction of magnetic material compared to core-shell particles, which will further improve the MR effect.²⁰ The novel polystyrene/Fe₃O₄ hollow microspheres exhibited a better MR effect than pure Fe₃O₄ MR fluid and a low apparent density of 1.5 g cm⁻³.²¹ An *et al.* prepared hollow Fe₃O₄ nanoparticles *via* a solvothermal method.²² The relative MR effect in shear viscosity reached 19 600% in a 343 kA m⁻¹ magnetic field. Diameter, wall thickness, and weight fraction of hollow Fe₃O₄ microspheres play important roles in the MR effect of MR fluid. However, the optimal diameter and wall thickness have not been investigated yet. Therefore, a systematic study of this hollow inner architecture was urgently required for both applications and fundamental interest.

CAS Key Laboratory of Mechanical Behavior and Design of Materials,
Department of Modern Mechanics, University of Science and Technology of China,
Hefei, Anhui, 230027, China. E-mail: xuansh@ustc.edu.cn, gongxl@ustc.edu.cn;
Tel: +86 551 63600419

† Electronic supplementary information (ESI) available. See DOI: 10.1039/c8sm00704g

With the help of theoretical progress, simulation has become an effective method to study MR fluid due to the advantages of low-cost and easy to adjust parameters. Several numerical methods, such as particle level dynamic simulation, the finite element method (FEM), computational fluid dynamics (CFD), and the Monte Carlo method, have been employed to study conventional MR fluid under different kinds of flows.^{23–26} A combination of experimental and simulation studies was carried out for poly-disperse MR fluid at the start of the shear flow.²⁷ The variations of yield stress could be explained by simulated microstructures and pair distribution functions. MR fluids with different initial microstructures under squeeze flow were analyzed by using particle level dynamic simulations.²⁸ The simulated normal force and yield compressive stress showed a linear dependence on the particle volume fraction and the square of magnetic field strength, which was in agreement with the experiments. In particular, particle level dynamic simulations were adopted to investigate the shear stress of hollow Fe_3O_4 based MR fluid at various shear rates.²⁹ Simulations matched well with experiments, which was helpful to understand the advantage of a hollow architecture. Therefore, simulation is able to reveal the MR mechanism at the microscopic level. This effective approach is also promising to find the optimal inner architecture of hollow Fe_3O_4 microspheres and guide the preparation of magnetic particles.

In this work, a novel particle level dynamic simulation was developed to find the best diameter and wall thickness of hollow Fe_3O_4 microspheres to improve the MR effect and reduce sedimentation. The simulation model including precise formulae for dipolar force, van der Waals force, and hydrodynamic drag force was firstly clarified. Typical evolutions of microstructures, shear stress, and magnetic potential energy in steady shear flow were investigated. The microstructures were analyzed both qualitatively and quantitatively. Then, the MR effects of hollow microspheres with different diameters, wall thicknesses, and weight fractions were systematically studied. The optimal diameter and wall thickness were obtained. A possible mechanism was developed to explain the variation of shear stress. Simulated viscosity data were discussed by using the Mason number. Finally, simulated shear stress as a function of magnetic field and shear rate matched well with experimental data.

Simulation model

Simulation set-up

Particle level dynamic simulations were carried out to investigate the microstructures and MR effects of MR fluid under steady shear flow. The simulation methodology was based on the dipole model. The MR fluid was regarded as a suspension of mono-disperse hard microspheres in a Newtonian fluid. A Cartesian coordinate system centered in a vertex of the simulation box was chosen, as shown in Fig. 1a. The simulation box was a cuboid with edge lengths of $L_x = L_y = 0.5L_z$. It was assumed that the matrix could enter hollow microspheres. But the matrix could not further flow into or out of the hollow microspheres during the transient shear flow. As the wall thickness and diameter of the particles changed, the weight fraction and volume fraction of hollow microspheres remained unchanged. The size of the simulation box also changed to ensure that the number of particles remained unchanged ($N \approx 2000$). Periodic boundary conditions were applied in the y - z plane and z - x plane, while shear boundary conditions were applied in the x - y plane. At the initial state, the MR fluid underwent a steady shear flow along the x -axis ($\dot{\gamma} = 100 \text{ s}^{-1}$). The shear stress could be expressed as σ_{zx} . Identical spherical particles were randomly distributed in the simulation box and moved along with the matrix. The Fe_3O_4 microspheres were free to move without the external field for 10^6 time steps to eliminate the overlaps among particles caused by random distribution. After that, an external magnetic field was applied along the z -axis. Then, the microstructure of the MR fluid started to evolve until the system reached homeostasis. The matrix was assumed to remain in steady shear state during the whole simulation. The MR effect was mainly ascribed to the interaction of microspheres.

Inter-particle forces

When a Fe_3O_4 microsphere is placed in a uniform magnetic field \mathbf{H} , the magnetic moment vector \mathbf{m}_i can be determined by an exponential function as:

$$\mathbf{m}_i = MV_i \frac{\mathbf{H}}{H} = M_s e^{-\frac{C_1}{H+C_2}} V_i \frac{\mathbf{H}}{H} \quad (1)$$

where M is the magnetization of Fe_3O_4 , $H = |\mathbf{H}|$, V_i is the volume of the target particle, $M_s = 71.7 \text{ emu g}^{-1}$ is the saturation

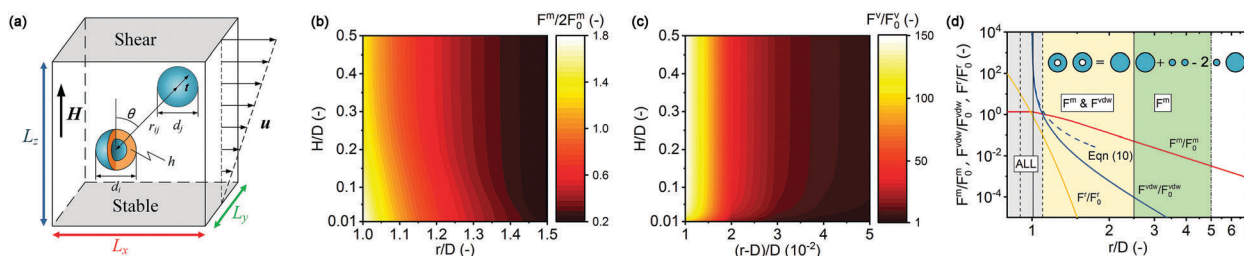


Fig. 1 (a) Schematic diagram of the simulation box. (b) Magnetic force and (c) van der Waals force between a pair of hollow microspheres as a function of r and H/D ($\theta = 0^\circ$). $F_0^m = 3\mu_0 m_i m_j / 4\pi d^4$ and $F_0^{vW} = 8A/3d$. m_i and m_j are magnetic moments of hollow microspheres. (d) The attenuation of inter-particle forces versus r . The two identical hollow particles ($H = 0.2D$) were assumed in a head-to-tail configuration along the z -axis. $F_0 = 3\mu_0 m_i m_j / 2\pi d^4 + 25F_0^{vW}/16$. Vertical lines indicated the truncation radii. Dashed dotted lines: magnetic dipolar force, solid lines: van der Waals force, and dashed lines: excluded volume force.

magnetization, and $C_1 = 265.7$ Oe and $C_2 = 39.0$ Oe are constants. C_1 measures the speed towards saturation. C_1 and C_2 together characterize the magnetization near zero magnetic field strength. In the super-paramagnetic state, the magnetic hysteresis loop is usually described by the Langevin function as:³⁰

$$M = M_s \left[\coth(x) - \frac{1}{x} \right] \quad (2)$$

where $x = M_s V_p H / k_B T$ and V_p represents the average volume of magnetic particles.³¹ Both functions match well with the experiments (Fig. S1, ESI[†]). In a sufficiently strong magnetic field, $x \gg 1$ and $H \gg C_2$. Eqn (1) and (2) can be derived from the same form:

$$M = M_s \left(1 - \frac{C_1}{H} \right) = M_s \left(1 - \frac{k_B T}{M_s V_p H} \right) \quad (3)$$

Constant C_1 approximately represent $k_B T / M_s V_p$. Both eqn (1) and (2) should express the same linear dependence on the magnetic field strength near the zero field region,

$$\left(\frac{dM}{dH} \right)_{H=0} = \frac{C_1}{C_2^2} e^{-\frac{C_1}{C_2}} = \frac{M_s V_p}{3k_B T} \quad (4)$$

Constant C_2 can be calculated from the transcendental equation.

All the microspheres are assumed to be magnetized instantly and equally in an MR fluid. The direction of the magnetic moment is parallel to the external field. At the same time, the magnetized particle also induces a magnetic field in the surrounding space as:

$$\mathbf{H}_i = -\frac{1}{4\pi r^3} [\mathbf{m}_i - 3(\mathbf{m}_i \cdot \hat{\mathbf{r}})\hat{\mathbf{r}}] \quad (5)$$

where \mathbf{r} denotes a spatial vector from the center of particle i to the spatial point. $r = |\mathbf{r}|$ and $\hat{\mathbf{r}} = \mathbf{r}/r$. If another particle is placed within the field \mathbf{H}_i , it will be magnetized by particle i . After several iterations, the magnetization of each microsphere is determined. Finally, the magnetic moment of a single particle is:

$$\mathbf{m}_i = M_s e^{-\frac{C_1}{|\mathbf{H}_{loc}| + C_2}} V_i \frac{\mathbf{H}_{loc}}{H_{loc}}, \quad \mathbf{H}_{loc} = \mathbf{H} + \sum_{j \neq i} \mathbf{H}_j \quad (6)$$

where \mathbf{H}_{loc}/H_{loc} indicates the direction of the magnetic moment vector. Linear superposition is applied here. Hollow and solid microspheres have the same bulk magnetization.²⁹ The magnetic moment of a hollow microsphere is in proportion to the volume of the solid part. Eqn (1) and (6) are also applicable to hollow particles.³²

The dipolar force of particle i exerted by particle j is:

$$\mathbf{F}_{ij}^m = \frac{3\mu_0}{4\pi r_{ij}^4} c_m [(-\mathbf{m}_i \cdot \mathbf{m}_j + 5\mathbf{m}_i \cdot \mathbf{t} \mathbf{m}_j \cdot \mathbf{t}) \mathbf{t} - (\mathbf{m}_i \cdot \mathbf{t}) \mathbf{m}_j - (\mathbf{m}_j \cdot \mathbf{t}) \mathbf{m}_i] \quad (7)$$

where r_{ij} stands for the distance between two particles. \mathbf{t} is the positional vector from particle i to particle j . The magnetic permeability of the matrix is considered equal to $\mu_0 = 4\pi \times 10^{-7}$ N A⁻². According to the theoretical analysis, a correction

factor c_m is introduced for adjusting the dipole model to two proximal particles.³³ c_m is calculated as:³⁴

$$c_m = \begin{cases} 1 + \left(3 - \frac{2r_{ij}}{d_{ij}} \right)^2 \left[\frac{0.6017}{1 + e^{(\theta| - 34.55)/12.52}} - 0.2279 \right] & r \leq 1.5d_{ij} \\ 1 & r > 1.5d_{ij} \end{cases} \quad (8)$$

Here, θ in degrees is the angle between \mathbf{t} and \mathbf{H} . d_i and d_j are the diameters of the particles, $d_{ij} = (d_i + d_j)/2$.

The van der Waals force between two microspheres can be expressed as:³⁵

$$\mathbf{F}_{ij}^{vdW} = \frac{8A}{3} L_{ij} d_i d_j \left[\frac{1}{4L_{ij}^2 - (d_i + d_j)^2} - \frac{1}{4L_{ij}^2 - (d_i - d_j)^2} \right]^2 \mathbf{t} \quad (9)$$

Here, $A = 3 \times 10^{-20}$ J is the Hamaker constant of Fe₃O₄ particles.³⁶ $L_{ij} = \max[r_{ij}, d_{ij} + h_{\min}]$, and $h_{\min} = 0.01d_{ij}$ were used.³⁷ Under the circumstance that two microspheres almost touch each other, eqn (9) evolves to the conventional form:

$$\mathbf{F}_{ij}^{vdW} = \frac{A}{24} \frac{d_i d_j}{d_{ij} (L_{ij} - d_{ij})^2} \mathbf{t} \quad (10)$$

Both the dipolar force and van der Waals force belong to electromagnetic force and satisfy the superposition principle. To compute the magnetic force, each hollow Fe₃O₄ microsphere is regarded as one solid sphere with the bulk magnetization M and a small solid sphere as large as the hollow part located at the same place with a negative bulk magnetization $-M$. The magnetic force between two hollow microspheres contains a big-big interaction, a pair of big-small interactions, and a small-small interaction. If $r \geq 1.5d_{ij}$, hollow microspheres are equivalent to solid ones with an effective magnetic moment. If $r < 1.5d_{ij}$, the point dipole model expressed a certain deviation compared to theoretical results.³³ Correction factor c_m is separately adopted in the three parts of magnetic force. The van der Waals force is calculated in a similar way. Both interactions are a function of H/D (Fig. 1b and c). Thin-walled microspheres exhibited a weaker relative magnetic force and a faster attenuation speed. The hollow architecture also expressed an influence on the van der Waals force for proximal particles.

To avoid the overlap among microspheres, the excluded volume force is taken into account as:

$$\mathbf{F}_{ij}^r = -\left(\zeta \frac{3\mu_0 m_{si} m_{sj}}{4\pi d_{ij}^4} + \mathbf{F}_{ij}^{vdW} \right) 10^{-10} \left(\frac{r_{ij}}{d_{ij}} - 1 \right) \mathbf{t} \quad (11)$$

where m_{si} and m_{sj} are the saturation magnetization of the target microspheres. $\zeta = 2$ is chosen in order to approximately cancel out with the dipolar force and van der Waals force when two particles were in a head-to-tail configuration along the field direction. Here the formula of the van der Waals force is chosen as eqn (10) to avoid complicated computing. This excluded volume force also works without the magnetic field. Fig. 1d shows that the inter-particle forces attenuate as the distance

increases. For simplicity, the truncation radius for the magnetic force, van der Waals force, and excluded volume force is $5d_{ij}$, $2.5d_{ij}$, and $1.1d_{ij}$, respectively. The truncation radii are large enough for simulations (Fig. S2, ESI†).

Particle–matrix interaction

The particle–matrix interaction contains hydrodynamic drag force, Brownian force, and buoyancy. The most frequently-used matrices (water, silicone oil) all belong to the Newtonian fluid. The laminar flow and turbulent flow can be distinguished by Reynolds number, which is defined as:

$$\text{Re} = \frac{\rho UL}{\eta} \quad (12)$$

Here, ρ and η are the density and viscosity of the matrix, respectively. U is the characteristic velocity. L is the characteristic length of the flow. In the rheological tests, the flow of the matrix is completely laminar flow ($\text{Re} = O(10^{-4})$). Therefore, the hydrodynamic drag force can be modeled by Stokes law:

$$\mathbf{F}_i^{\text{h}} = -3\pi\eta d_i c_{\text{h}} (\mathbf{v}_i - \mathbf{u}_i) \quad (13)$$

where $\mathbf{v}_i - \mathbf{u}_i$ is the velocity of particle i relative to the matrix. In concentrated MR fluid, the surrounding particles will enlarge the drag force. c_{h} is a correction factor for \mathbf{F}_i^{h} , presented by He *et al.* as:³⁸

$$c_{\text{h}} = \frac{1 + 5.81\varphi_{\text{a}}}{(1 - \varphi_{\text{a}})^3} + 0.48 \frac{\sqrt[3]{\varphi_{\text{a}}}}{(1 - \varphi_{\text{a}})^4} + \varphi_{\text{a}}^3 \text{Re} \left[0.95 + \frac{0.61\varphi_{\text{a}}^3}{(1 - \varphi_{\text{a}})^2} \right] \quad (14)$$

Here, $\varphi_{\text{a}} = \varphi/S$ is the apparent volume fraction. φ is the volume fraction of the MR fluid and S is the solid proportion of hollow microspheres. Due to the extremely low Reynolds number, the last term in eqn (14) is negligible.

The random Brownian force has a great influence on nanospheres ($D \approx 10$ nm). For the hollow microspheres in this study ($D \approx 100$ nm), the intensity of the magnetic force is much stronger than the thermal motion and buoyancy (Fig. S5, ESI†). Simulation results with Brownian force are very close to those not considering Brownian force. Thus the Brownian force, gravity, and buoyancy of hollow Fe_3O_4 microspheres are neglected.

The validity of the particle–matrix model is characterized by Knudsen number, which is defined as:

$$\text{Kn} = \frac{\lambda}{L} \quad (15)$$

where λ is the mean free path of the matrix molecules. L is the characteristic length. $\text{Kn} \leq 0.1$ means that the matrix can be regarded as a continuous medium.³⁹ Liquid molecules in MR fluid are not free to move. Thus, λ is an approximate to the cube root of molecule volume:

$$\lambda \approx \sqrt[3]{\frac{M}{\rho_0 N_{\text{A}}}} \quad (16)$$

Here, M is the molecular mass of the matrix. N_{A} is Avogadro's number. For an MR fluid based on water, the particle–matrix

model applies to microspheres with a diameter $D \geq 10$ nm. For the MR fluid based on silicone oil ($\eta = 0.01$ Pa s $M = 1.2$ kg mol⁻¹), the aforementioned model applies to microspheres with a diameter $D \geq 130$ nm.

Equation of motion

Due to the super-paramagnetic property of Fe_3O_4 microspheres, the magnetic torque acting on a single particle is so exiguous that the rotational motion is neglectable. Particle inertia has little effect on particle motion in homeostasis. However, on applying an external field, the particles moved with large accelerations. To avoid the leap in velocities and confirm the convergence of the simulation, the inertia of the microspheres is taken into account during the calculation. Considering the forces mentioned above, the equation of motion is constructed as:

$$\sum_{j \neq i} (\mathbf{F}_{ij}^{\text{m}} + \mathbf{F}_{ij}^{\text{vdW}} + \mathbf{F}_{ij}^{\text{r}}) + \mathbf{F}_i^{\text{g}} + \mathbf{F}_i^{\text{h}} = m_{\text{p}i} \mathbf{a}_i \quad (17)$$

where $m_{\text{p}i}$ is the mass of particle i . The modified velocity-Verlet algorithm is employed to solve eqn (17), in which the empirical parameter is chosen as 0.65.⁴⁰ The magneto-induced stress tensor $\boldsymbol{\sigma}$ and magnetic potential energy U_{m} are presented as:

$$\boldsymbol{\sigma} = \frac{1}{V} \sum_i \left[\sum_{j>i} \mathbf{r}_{ij} \mathbf{F}_{ij} - m_{\text{p}i} (\mathbf{v}_i - \mathbf{u}_i) (\mathbf{v}_i - \mathbf{u}_i) \right] \quad (18)$$

$$U_{\text{m}} = \mu_0 \sum_i \left[-\mathbf{m}_i \cdot \mathbf{H} + \sum_{j>i} \frac{1}{4\pi r_{ij}^3} (\mathbf{m}_i \cdot \mathbf{m}_j - 3\mathbf{m}_i \cdot \mathbf{t}_{ij} \cdot \mathbf{t}_{ij}) \right] \quad (19)$$

Here, V is the volume of the simulation box. \mathbf{F}_{ij} is the total inter-particle force between these two particles. U_{m} consists of the particle–external field section and inter-particle section. Previously we found that the deviation between the point dipole model and theoretical results in magnetic energy ($\leq 5\%$) is much smaller than that in magnetic force ($\leq 33\%$).³⁴ Thus the point dipole approximation is still applied in eqn (19). The particle pair distribution function is employed to investigate the microstructures quantitatively. As a consequence of the spherical and azimuthal symmetries in the particulate interactions, this function can be easily obtained using the following equation:⁴¹

$$g(r, \theta) = \frac{V}{N^2} \left\langle \sum_i \sum_{j \neq i} \delta(r - r_{ij}) \delta(\theta - \theta_{ij}) \right\rangle \quad (20)$$

where N represents the number of particles and the bracket means volume average. The radial distribution function and angular distribution function can be obtained simply by the integration of eqn (20):

$$g(r) = \int_0^\pi g(r, \theta) \sin \theta d\theta \quad (21)$$

$$g(\theta) = \int_0^{R_c} 4\pi r^2 g(r, \theta) dr \quad (22)$$

where the truncation radius is $R_c = 5D$.

Experimental verifications

In order to testify the accuracy of the simulations, a hollow Fe_3O_4 microsphere-based MR fluid was prepared. The shear stress in a magnetic field sweep was compared to the simulation results.

Chemicals

Citric acid trisodium salt dihydrate ($\text{C}_6\text{H}_5\text{Na}_3\text{O}_7 \cdot 2\text{H}_2\text{O}$), urea ($\text{CO}(\text{NH}_2)_2$), iron(III) chloride hexahydrate ($\text{FeCl}_3 \cdot 6\text{H}_2\text{O}$), polyacrylamide 3 000 000 (PAM, $(\text{C}_3\text{H}_5\text{NO})_n$), and polyvinylpyrrolidone (PVP, $(\text{C}_6\text{H}_9\text{NO})_n$) were used in the synthesis of hollow Fe_3O_4 microspheres. All the reactants were purchased from Sinopharm Chemical Reagent Co, Ltd (analytical graded) and used without further purification.

Preparation of hollow Fe_3O_4 microspheres

The hollow Fe_3O_4 microspheres were prepared *via* a hydrothermal method.³³ Firstly, 16 mmol $\text{C}_6\text{H}_5\text{Na}_3\text{O}_7 \cdot 2\text{H}_2\text{O}$, 24 mmol $\text{CO}(\text{NH}_2)_2$, and 8 mmol $\text{FeCl}_3 \cdot 6\text{H}_2\text{O}$ were dissolved in 80 ml secondary distilled water. The mixture was vigorously stirred. Then, 0.6 g PAM and 0.2 g PVP were mixed into the solution. The mixture was kept stirring at 300 rpm for about 1 h to ensure that the reagents dissolved completely. The solution was transferred into a 100 ml reaction kettle and maintained at 200 °C for 12 h. After cooling down to room temperature, the black precipitate was ultrasonically washed with distilled water and ethanol 4 times. Finally, the precipitate was dried in a vacuum desiccation oven for 24 h to obtain pure hollow Fe_3O_4 microspheres. In addition, the above hollow microspheres were dispersed into water and silicone oil (10 cSt). MR fluid samples with a weight fraction of 5 wt%, 10 wt%, and 20 wt% for each kind of matrix were prepared.

Characterization

The microscopic morphology of the microspheres was observed by using a transmission electron microscope (TEM) (JEM-2100F, JEOL Co., Japan) with an accelerating voltage of 200 kV. The magnetization property at room temperature was characterized *via* a magnetometer (SQUID VSM, Quantum Design Co., America) with an applied field sweep from -30 kOe to 30 kOe.

The MR effect of MR fluid based on the hollow Fe_3O_4 was measured by using a commercial rheometer (Physica MCR 302, Anton Paar Co., Austria). Typically, the samples were imposed between the upper plate (PP20/MRD) and the base bed. The parallel gap was fixed as 0.8 mm. Each test was conducted at 25 °C. The magnetic field sweep tests were carried out at a constant shear rate of 100 s^{-1} . A pre-shear was carried out for 30 s to ensure that the samples remain in the steady shear state. Then the magnetic flux density linearly increased *versus* time from 0 T to 0.9 T. In the shear rate sweep tests, the external magnetic field was set at 0 T, 0.11 T, 0.22 T, 0.44 T, and 0.88 T, respectively. The shear rate logarithmically increased with time from 0.1 s^{-1} to 100 s^{-1} .

Results and discussion

Typical evolution of microstructures and shear stress in steady shear flow

The microstructures of the MR fluid had a great influence on the MR effect. Firstly, the typical rearrangement of hollow Fe_3O_4 microspheres in steady shear flow was investigated. Meanwhile, the magneto-induced shear stress and potential energy density were analyzed. In this section, a steady uniform magnetic field $B = 0.88 \text{ T}$ was chosen as an example. This magnetic field could ensure that the MR fluid exhibited the maximum MR effect. The shear rate was set at 100 s^{-1} . The diameter and wall thickness of the hollow magnetic microspheres were set at 300 nm and 60 nm, the same as the samples prepared in experiments. The weight fraction of Fe_3O_4 was 20 wt%. The MR fluids could exhibit an MR effect on the order of milliseconds, which corresponded to a shear strain $\gamma = 1$. In order to reduce the time consumption, the simulation terminated as the shear strain reached $\gamma = 2$. The results of shear stress were the average of 3 times.

Fig. 2 shows the snapshots of microstructures in an MR fluid at different shear strains. The hollow microspheres were plotted as solid spheres here. All the hollow Fe_3O_4 microspheres were chaotic at the beginning of the simulation. Then the magnetic phase in the MR fluid tended to align along the magnetic field direction (z -axis) to decrease the magnetic energy. The microspheres rapidly formed many chains with different lengths ($\gamma = 0.04$). Furthermore, the one-dimensional microstructures inclined to the shear direction ($\gamma = 0.25$). The aggregation along the flow direction (x -axis) started. When the shear strain became large enough, particle chains were destroyed by the hydrodynamic force and rebuilt by the magnetic dipolar force. During the destruction and recombination process, the particulate chains drew close in the lateral direction (y -axis) as the matrix flowed ($\gamma = 1.00$). Several cluster microstructures appeared in the simulation box. The particle aggregates moved to several separated planes when the shear strain reached $\gamma = 2.00$. The separation distance of two particle lamellae is larger than the truncation radius of magnetic dipolar force. Due to the periodic boundary conditions, the isolated particle belongs to the cluster microstructures in the next simulation box. There is seldom a single Fe_3O_4 microsphere in the MR fluid.

To characterize the field-induced aggregation process, the evolution of shear stress, magnetic potential energy per particle ($|U_m|/N$), and number of neighbors per particle (N_{near} , within a center-to-center distance of $2.5D$) were plotted as shown in Fig. 3a and b. The evolution was divided into four parts. The shear stress started with an approximately linear increase, which was similar to the linear elastic region of solids at small strains (Zone I and II). When the shear strain reached 0.25, the shear stress increased with fluctuation in a lower speed (Zone III). Then, the shear stress started to fluctuate and finally reached homeostasis (Zone IV). The aggregation on the x -axis and y -axis contributed to the shear stress. The average stress from $\gamma = 1$ to the end of the simulation could represent the macroscopic stress.

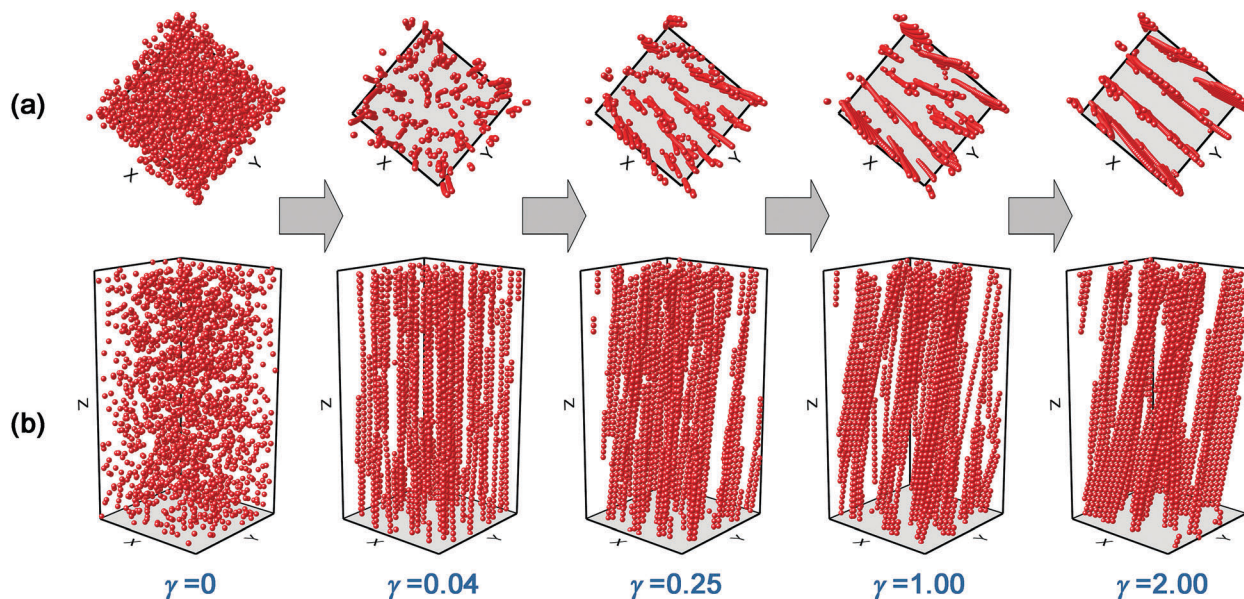


Fig. 2 Microstructures of MR fluids based on the hollow Fe_3O_4 microspheres at different shear strains: $\gamma = 0, 0.04, 0.25, 1.00,$ and 2.00 . (a) Top view, (b) perspective view.

Due to the particle–external field interaction, each hollow Fe_3O_4 microsphere gained an initial magnetic potential energy of -4.42×10^{-15} J after the simulation started, which is not reflected in Fig. 3b. Then the energy density sharply decreased (Zone I), which was much faster than the increase of shear stress. This phenomenon was mainly ascribed to the aggregation along the z -axis. After that, the energy density gradually decreased to the plateau. N_{near} generally increased as the shear strain increased to $\gamma = 1.00$. The slope gradually decreased from Zone I to Zone III, which was associated with the aggregation along the z -axis, x -axis, and y -axis, respectively. In Zone IV, N_{near} reached homeostasis. According to eqn (7) and (18), close ranged microspheres had a greater contribution to the stress tensor. Larger N_{near} was helpful for generating larger shear stress.

At the initial state, both the distribution functions were horizontal lines located at $G = 1$ (Fig. 3c and d), consistent with the random distribution. Then, an obvious main peak appeared at the position $r/D = 1$ in the radial distribution function. Several other peaks were at the positions $r/D = 1.75, 1.95, 2.15, 2.65,$ and 2.95 . The position of the peaks almost never changed while the peak values slightly increased as the shear strain increased. The peak value in the radial distribution function reflected the tightness of particle aggregates. Magnetic microspheres drew close to each other and formed some short-range ordered microstructures soon after applying the external field. The tightness of the aggregates kept growing until homeostasis. In the angular distribution function curves, there were two peaks at $\theta = 0-3^\circ$ and $\theta = 177-180^\circ$. From Zone I to Zone IV, the peak value remarkably decreased from 100 to 17.8. The two troughs at $\theta = 45^\circ$ and $\theta = 135^\circ$ developed into a low plateau. The angular distribution function reflected the inclined angle of the particle chains, which had a great effect on the shear stress. Particle clusters tended to incline at an angle between 0° and 30° . Meanwhile, microspheres in the horizontal alignment significantly decreased.

MR effect of MR fluids based on hollow microspheres with different diameters and wall thicknesses

A. For a diluted MR fluid. It was important to understand how the shear stress and microstructures varied if the diameter (D) and wall thickness (H) of the hollow Fe_3O_4 microspheres changed. An MR fluid with a weight fraction of 20 wt% was chosen as an example due to the common adoption in rheological tests. Here, the diameter of the microspheres was set at $D = 100$ nm, 300 nm, 500 nm, and 1000 nm. It was difficult to prepare hollow Fe_3O_4 nanoparticles. Hollow spheres smaller than $D = 100$ nm were not taken into account. The wall thickness increased from $H = 10$ nm to $H = 0.5D$. Thus the

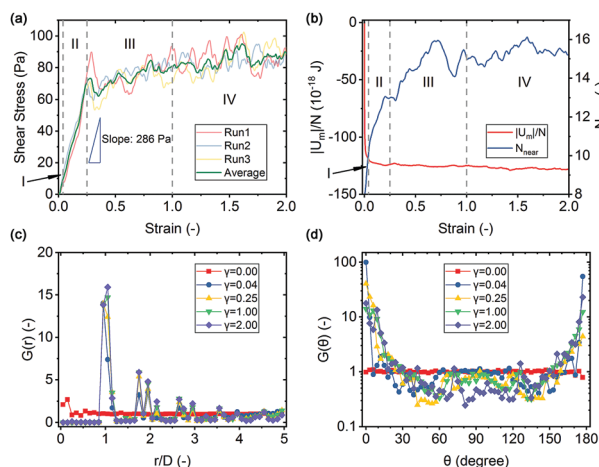


Fig. 3 (a) Shear stress versus shear strain curves from each performance of the program and the averaged value. (b) Magnetic potential energy and number of neighbors per particle versus shear strain. (c) Radial distribution function and (d) angular distribution function at different shear strains.

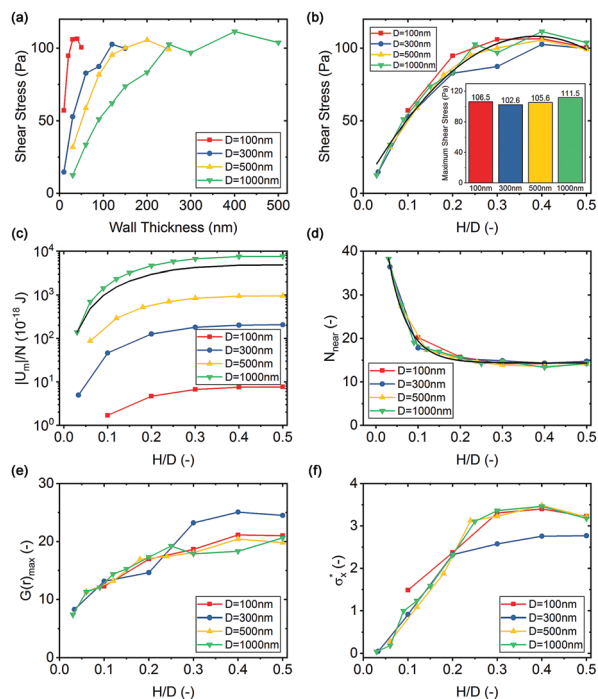


Fig. 4 Shear stress versus wall thickness curves from 20 wt% hollow Fe_3O_4 MR fluids with different diameters. The abscissa in (a) real units and (b) dimensionless units. (c) Magnetic potential energy per particle, (d) number of neighbors per particle, (e) peak value of radial distribution function, and (f) σ_x^* versus dimensionless wall thickness.

solid proportion of hollow microspheres S varied from 16.9% to 100%. The external magnetic field was fixed at 0.88 T while the shear rate was set at 100 s^{-1} .

Fig. 4a shows the shear stress as a function of wall thickness. At the same diameter, the shear stress firstly increased as the wall thickness increased until $H = 0.4D$ and then slightly decreased near the maximum H . If the wall thickness remained unchanged, smaller hollow microspheres expressed a higher shear stress. All the curves collapsed onto a master curve in dimensionless abscissa unit H/D (solid line in Fig. 4b). Shear stress had a quadratic dependence on H/D , which was $\tau = -695(H/D - 0.39)^2 + 110$. The optimal wall thickness obtained from the master curve was $H = 0.39D$, while the optimal diameter was $D = 1000 \text{ nm}$. Magnetic potential energy per particle reflected the intensity of inter-particle dipolar force (Fig. 4c). $|U_m|/N$ increased as the wall thickness increased, which was faster than the increase of the square of hollow microsphere volume (solid line). This was because the tightness of the particle aggregates increased accordingly. Under the same H/D , $|U_m|/N$ was in proportion to the cube of particle diameter. In Fig. 4d, all the N_{near} curves collapsed onto an exponential decayed master curve. Although the diameter changed, hollow microspheres with the same H/D formed similar microstructures. Particle aggregates enlarged or reduced in proportion. N_{near} was only associated with the apparent volume fraction ϕ_a . The radial distribution function (Fig. 4e) and the following angular distribution function (Fig. 4f) were obtained from microstructures when the instantaneous shear stress was equal to the

average shear stress. $G(r)_{\text{max}}$ did not grow linearly with the apparent volume fraction. The diameter of the particles had a great influence on $G(r)_{\text{max}}$. The peak values mainly achieved a maximum at a certain wall thickness $H = 0.4D$. The orientation of the particle chains played an important role in MR effects. The magneto-induced shear stress between two microspheres as a function of θ and S is shown in Fig. S7 (ESI[†]). The contribution of the particle chain orientations to shear stress could be expressed by the following equation instead of the peak value of the angular distribution function.

$$\sigma_x^* = \int_0^\pi r \cos \theta \frac{F_x^m}{F_0^m d^4 r^{-3}} G(\theta) \sin \theta d\theta \quad (23)$$

Here, $r \cos \theta F_x^m / F_0^m d^4 r^{-3}$ referred to the dimensionless shear stress between a pair of particles. The main contribution of shear stress was from magnetic interactions. Eqn (23) could reflect the quality of the orientation of the particle chains from the point of magnetic force without the influence of particle diameter and magnetic field strength. If the microspheres formed cluster or lamellar microstructures, σ_x^* could be regarded as the total contribution of particle chains in different directions. The influence of the azimuth was negligible, because there were few interactions between particle lamellae. σ_x^* reached the maximum at $H = 0.4D$. $D = 300 \text{ nm}$ microspheres presented an advantage in radial distribution function but a disadvantage in particle chain orientations. In summary, the maximum shear stress of $D = 100 \text{ nm}$ microspheres was larger than that of $D = 300 \text{ nm}$ microspheres because of the stronger van der Waals force. $D = 1000 \text{ nm}$ microspheres possessed larger inertia, so the microstructures were difficult to be destroyed by the matrix. Particle aggregates could remain in the optimal orientation for a long time, thus $D = 1000 \text{ nm}$ microspheres exhibited the best MR effect. Thin-walled hollow microspheres presented a poor MR effect mainly because of the weak magnetic interaction. The σ_x^* of thin-walled hollow microspheres was also not conducive to the shear stress. The intensity of magnetic force increased due to the increasing wall thickness. The particle aggregates also became more compact. At the same time, ϕ_a decreased, leading to a decrease in N_{near} . The competition of the aforementioned factors led to an increase in shear stress versus H/D . When the wall thickness was $H > 0.4D$, $|U_m|/N$ and N_{near} reached a plateau. Shear stress slightly decreased mainly due to the change in $G(r)_{\text{max}}$ and particle chain orientations. The macroscopic shear stress was the result of competition among the magnetic interactions, number of neighbors, tightness of the microstructures, and orientation of the particle chains.

The change of wall thickness also had a great influence on the microstructures. Fig. 5 shows snapshots of a 20 wt% MR fluid based on microspheres with $D = 300 \text{ nm}$ and different wall thicknesses at the end of the simulation. Here the hollow microspheres were plotted as solid ones. As the wall thickness changed, the size of the simulation box changed proportionately in order to ensure that the number of particles remains unchanged. Each subfigure had a different display scale. When the wall thickness was $H = 10 \text{ nm}$, hollow particles formed thick lamellar microstructures. If the wall thickness increased to

$H = 30$ nm, the particle aggregates became monolayered. For $H = 60$ nm hollow microspheres, the lamellar microstructures transferred into separated cluster microstructures. Each part exhibited different inclined angles but still located in several separated planes. When the wall thickness further increased, particle chains tended to align vertically and the aggregation along the y -axis became weaker. For solid microspheres, some nearby cluster microstructures were even located in different planes. Microspheres with larger wall thickness had a stronger magnetic interaction. Therefore, the microstructure would not be easily destroyed or driven by shear flow. The stability of the microstructures caused a poor quality in the orientation of the particle clusters.

B. For a concentrated MR fluid. In order to achieve a higher MR effect, MR fluids with higher weight fraction (≈ 40 wt%) are usually adopted in applications. In a hollow sphere system, the apparent volume fraction must satisfy the closest packing $\varphi_a < 74\%$. It was reported in the literature that concentrated MR fluids could also exhibit a shear thickening phenomenon under a certain magnetic field and a certain shear rate.⁴² Squeeze and friction among hollow microspheres exhibited a great influence on the shear stress when $\varphi_a > 50\%$. Without the consideration of the friction force, eqn (11) would lead to an inaccuracy in simulations. The wall thickness was set from $H = 0.06D$ to $H = 0.5D$, while the corresponding φ_a was set from 11.5% to 36.2% to avoid the aforementioned problem. In a 40 wt% MR fluid, the shear stress exhibited similar characteristics to a 20 wt% MR fluid (Fig. S8, ESI[†]). In Fig. 6a, the shear stress reached the maximum approximately when $H = 0.4D$. The peak value from each curve was approximately double that of a 20 wt% MR fluid compared to Fig. 4b. All the curves also collapsed onto a quadratic master curve, which was expressed as $\tau = -1500(H/D - 0.35)^2 + 186.5$. The optimal wall thickness decreased to $H = 0.35D$, while the optimal diameter was $D = 100$ nm. $|U_m|/N$ increased along with the wall thickness (Fig. 6b). Interestingly, although the volume fraction of a 40 wt% MR fluid was higher, the $|U_m|/N$ was slightly lower

than a 20 wt% MR fluid. The intensity of the magnetic interaction per particle in concentrated MR fluid was unusually weakened. In Fig. 6c, N_{near} versus H/D curves still collapsed onto an exponential decayed master curve. The N_{near} values of the curves were approximately double those in a 20 wt% MR fluid. The decline speed of N_{near} in the concentrated MR fluid was slower than that in the diluted MR fluid. In Fig. 6d, the maximum value of the $G(r)_{\text{max}}$ curves appeared at $H = 0.4D$. In a concentrated MR fluid, the microspheres form thick lamellar microstructures and the distance between lamellae is smaller than the truncation radius. In order to analyze the orientation of particle chains, the azimuth should be taken into account. σ_x^* fluctuates around the average value without an obvious trend, which is not plotted here. In summary, the high shear stress of $D = 100$ nm hollow microspheres could be attributed to the van der Waals force. If the diameter further decreased, the Brownian motion would disturb the particle aggregation. Smaller nanosphere would not exhibit a larger shear stress, which has been proved in the literature.³³ When $H \leq 0.3D$, the main influencing factors on shear stress were the dramatically changed $|U_m|/N$ and N_{near} . When the wall thickness drew close to $H = 0.5D$, the above factors reached a plateau. The decrease in $G(r)_{\text{max}}$ led to a slight drop in shear stress. The peaks in the shear stress curves were the result of competition among the magnetic forces, number of neighbors, and tightness of the microstructures.

Microstructures of a 40 wt% MR fluid based on microspheres with $D = 300$ nm and different wall thicknesses are shown in Fig. 7. If the wall thickness reached $H = 0.033D$, corresponding to the apparent volume fraction 61.7%, hollow microspheres always contact each other. No obvious microstructures could be identified from the snapshot. This situation is not shown in Fig. 6. The lamellar microstructures became thinner as the wall thickness became larger. When $H \geq 0.3D$, defects occurred in the lamellae. This phenomenon decreased the tightness of the particle aggregates thus further reducing the $G(r)_{\text{max}}$ (Fig. 6d).

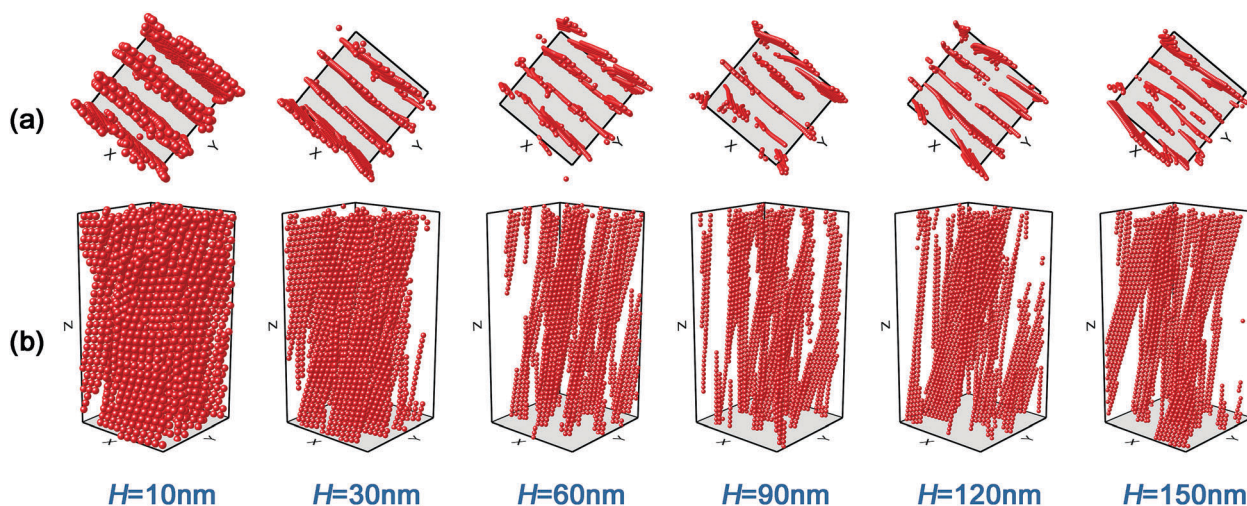


Fig. 5 Snapshots of 20 wt% MR fluids based on microspheres with different wall thicknesses. (a) Top view, (b) perspective view.

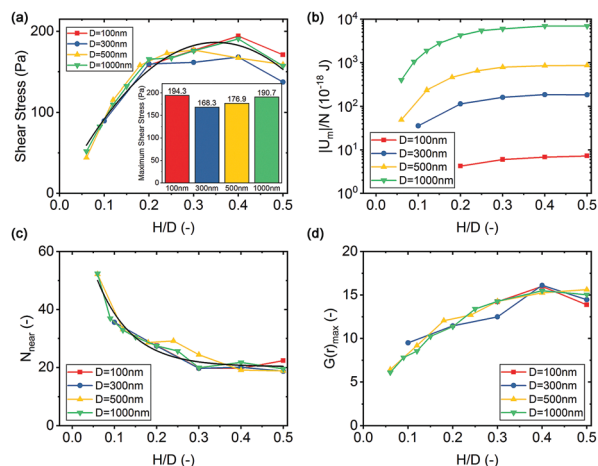


Fig. 6 (a) Shear stress versus dimensionless wall thickness curves from 40 wt% hollow Fe_3O_4 MR fluids with different diameters (inset: the peak value of each curve). (b) Magnetic potential energy per particle, (c) number of neighbors per particle, and (d) peak value of the radial distribution function as a function of dimensionless wall thickness.

Mason number

In this section, the Mason number is determined for the hollow Fe_3O_4 microsphere suspension. This dimensionless number can produce a collapse of viscosity data at various magnetic field strengths and shear rates. Klingenberg *et al.* defined the Mason number for MR fluid as the ratio of hydrodynamic drag force and magnetic polarization force.⁴³

$$M_n = \frac{F^H}{F^M} \quad (24)$$

$$\begin{cases} F^H = \frac{3}{2}\pi\eta d^2 c_h \dot{\gamma} \\ F^M = \frac{3\mu_0\mu_c m_i^2}{4\pi d_i^4} \end{cases} \quad (25)$$

where the relative magnetic permeability of the continuum matrix $\mu_c \approx 1$. The magnetic moment m_i is expressed as $m_i = V\langle M_{\text{sph}} \rangle = \pi d_i^3 \langle M_{\text{sph}} \rangle / 6 = \pi d_i^3 M / 6$, where $\langle M_{\text{sph}} \rangle = \langle M \rangle / \varphi_a$. $\langle M \rangle$ is the magnetization of the suspension. In this way, M_n included the magnetization of microspheres both at low and high field values. When the particle diameter and wall thickness were changed, $\langle M \rangle$ and the weight fraction of Fe_3O_4 remained unchanged. By inserting the expression of m_i into eqn (25), M_n is finally expressed as:⁴⁴

$$M_n = \frac{72\eta c_h \dot{\gamma}}{\mu_0 M^2 S^2} \quad (26)$$

where M is the magnetization of Fe_3O_4 in eqn (1). Each parameter in eqn (26) can be determined from experiments or simulations. The mason number defined in this way allows the influence of the matrix viscosity, shear rate, external field, and particle architecture to be described by using only one dimensionless number. The simulation results $\eta_{\text{app}}/\eta_\infty = f(M_n)$ for all kinds of microspheres and different weight fractions collapse onto a single master curve (Fig. 8). The slope of the master curve in a log-log coordinate is -0.59 . Here η_∞ is obtained from $D = 300$ nm, $H = 60$ nm hollow Fe_3O_4 microspheres. It is assumed that solid proportion S doesn't significantly influence the η_∞ under the same weight fraction. For most ranges of S , the viscosity monotonously decreased with Mason number. Some deviations appear only when the wall thickness is close to $H = 0.5D$. This phenomenon could be attributed to the increasing defects in the microstructures. A similar collapse of viscosity data was also observed in the literature.⁴⁴ It is significant that the nonlinear magnetization in this article originates from the different physical characteristics of magnetic particles instead of the change of magnetic field strengths.

Experimental results

Typical TEM images of hollow Fe_3O_4 particles (Fig. 9a) showed that the microspheres were spherical and monodispersed.

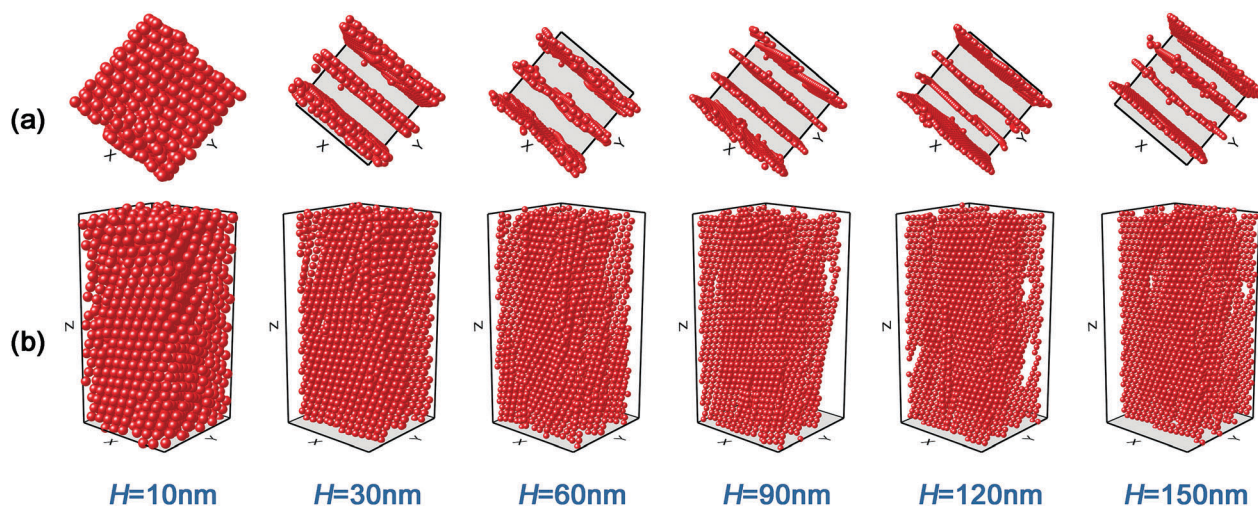


Fig. 7 Snapshots of a 40 wt% MR fluid based on microspheres with different wall thicknesses. (a) Top view, (b) perspective view.

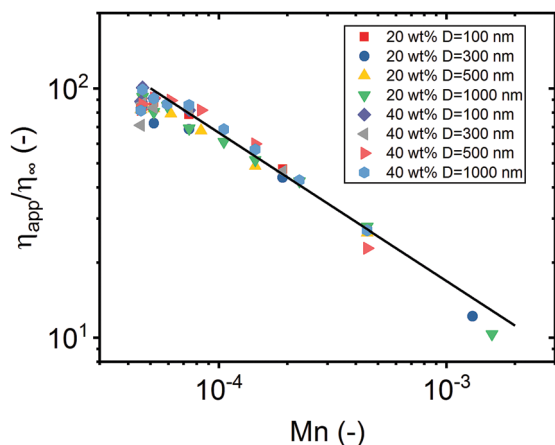


Fig. 8 Dimensionless viscosity as a function of Mason number for hollow Fe_3O_4 microspheres with different diameters, wall thicknesses, and weight fractions.

The hollow feature was obvious in each particle. The diameter was estimated to be 300 nm while the wall thickness was approximately 60 nm (Fig. 9b). Fig. 9c shows the magnetic hysteresis loop of hollow Fe_3O_4 samples. The microspheres presented excellent super-paramagnetic properties with a saturation magnetization of 71 emu g^{-1} and zero residual

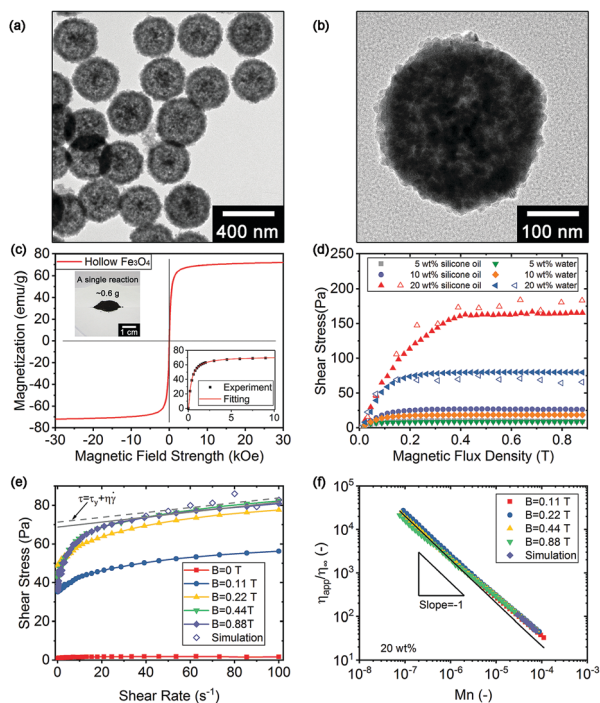


Fig. 9 (a and b) TEM images of hollow Fe_3O_4 microspheres. (c) Magnetic hysteresis loops of particles. (Inset: fitting results of hysteresis loops between 0 and 10 kOe.) (d) Shear stress as a function of magnetic flux density of an MR fluid based on the hollow Fe_3O_4 microspheres. Solid symbols: experiments, open symbols: simulations. (e) Flow curves of MR fluids in different external magnetic fields. Open symbols stand for simulation results. Solid and dashed line represents the prediction of dynamic yield stress from experiments and simulations, respectively. (f) Dimensionless viscosity *versus* Mason number for various magnetic fields.

magnetism and coercive force. The fitting curve of eqn (1) was very close to the experimental results (inset graph), of which the R -square was 0.9998. Fig. 9d shows the shear stress of a MR fluid as a function of magnetic flux density. The magneto-induced shear stress firstly increased along with the external field and then reached a plateau after 0.4 T, which was similar to the hysteresis loop in the first quadrant. Typically, the shear stress curves of a 20 wt% MR fluid based on water and silicone oil in the magnetic field sweep agreed well with the simulation results. However, the simulations slightly overestimated the shear stress of the MR fluid based on silicone oil while disappreciated the shear stress of the MR fluid based on water. This was because the MR fluid formed some large-scale anisotropic microstructures. Such microstructures were not reflected in the simulation due to the restriction of the calculation scale. Further work should be done to improve the accuracy of the simulations. Shear stress as a function of shear rate for a 20 wt% MR fluid at various magnetic flux densities is shown in Fig. 9e. The MR fluid possessed a static yield stress when the shear rate was $\dot{\gamma} \rightarrow 0$. The shear stress firstly showed a rapid growth and then a linear growth *versus* shear rate. The samples exhibited typical characteristics of Bingham fluids at a high shear rate. The flow curves can be described as:

$$\tau = \tau_0 + \eta_p \dot{\gamma} \quad (27)$$

where τ_0 stands for the dynamic yield stress and η_p represents the plastic viscosity. This parameter can be obtained from the linear fitting of flow curves at high shear rates. The τ_0 values under a magnetic field of 0.11 T, 0.22 T, 0.44 T, and 0.88 T were 46.9 Pa, 64.7 Pa, 68.7 Pa, and 69.3 Pa, respectively. Simulations of the MR fluid at a shear rate from 40 s^{-1} to 100 s^{-1} in a 0.88 T magnetic field were carried out to compare with experiments. The simulated dynamic yield stress $\tau_0 = 71.3$ Pa was very close to experiments, the dash line in Fig. 9e. The dimensionless viscosity could be expressed as:

$$\frac{\eta_{\text{app}}}{\eta_{\infty}} = \frac{\eta_p}{\eta_{\infty}} + \frac{\tau_y}{\eta_{\infty} \dot{\gamma}} \quad (28)$$

At a very high shear rate in the absence of a magnetic field, $\eta_p = \eta_{\infty}$. According to eqn (26), the apparent viscosity yields:⁴⁵

$$\frac{\eta_{\text{app}}}{\eta_{\infty}} = 1 + B_n = 1 + M_n^* M_n^{-1} \quad (29)$$

Here, $B_n = \tau_y / \eta_{\infty} \dot{\gamma}$ is the Bingham number and $B_n \propto M_n^{-1}$. Dimensionless viscosity from experiments and simulations as a function of Mason number collapsed onto a single master curve, as shown in Fig. 9f. $M_n^* = 2 \times 10^{-3}$ was obtained from the fitting curve. Some deviations from the fitting curve originated from the assumption that $\eta_p = \eta_{\infty}$. The influence of η_p was obvious only under large Mason numbers. Based on the above results, the present simulations coincided well with experiments.

Conclusions

In this work, a particle level dynamic simulation was carried out to investigate the influence of particle diameter, wall

thickness, and weight fraction on the MR effect of hollow magnetic microspheres. An accurate model of dipolar force, van der Waals force, and hydrodynamic drag force was adopted to obtain accurate results. The microstructures of the MR fluid were analyzed both qualitatively and quantitatively. Shear stress tests in magnetic field sweep and shear rate sweep confirmed the accuracy of the simulation.

In the typical steady shear flow, the sharp drop in magnetic energy reflected the aggregation along the field direction. The linear growth and fluctuant growth region in the shear stress–strain curves were corresponding to the inclination of particle chains and the aggregation along the y -axis, respectively. Hollow microspheres evolved from a uniform distribution to chain-like microstructures. Finally, particle chains inclined and formed clusters located in several separated planes, which led to the homeostasis of shear stress. The tightness of microstructures kept growing during the three steps of aggregations. Cluster microstructures tended to incline at an angle between 0 and 30° as the system reached homeostasis. Microspheres in horizontal alignment significantly decreased at the same time.

For hollow Fe₃O₄ microspheres with different diameters and wall thicknesses in a 20 wt% MR fluid, all the shear stress curves presented a quadratic relationship with H/D . The optimal wall thickness obtained from the master curve was $H = 0.39D$, while the optimal diameter was $D = 1000$ nm. The growing magnetic interaction promoted shear stress while the reducing number of neighbors per particle hindered shear stress by increasing the wall thickness. If the wall thickness was $H \geq 0.3D$, the above factors reached a plateau. The radial distribution function and orientation of particle chains became the dominant factors in shear stress. Hollow microspheres transformed from thick lamellar microstructures to monolayered lamellar microstructures and finally formed separated clusters by increasing the wall thickness. Simulation results from a 40 wt% MR fluid exhibited similar characteristics. The optimal wall thickness obtained from the master curve was $H = 0.35D$. The optimal diameter was $D = 100$ nm. For $D = 100$ nm microspheres, the van der Waals force made a great contribution to shear stress. The maximum shear stress of a 40 wt% MR fluid was double that of a 20 wt% MR fluid. The simulated viscosity data *versus* Mason number for microspheres with different diameters, wall thicknesses, and weight fractions collapsed onto a single master curve. This dimensionless number was proven to be valuable for describing MR fluids with different physical characteristics.

Conflicts of interest

There are no conflicts to declare.

Acknowledgements

Financial support from the National Natural Science Foundation of China (Grant No. 11572309 and 11572310) is gratefully

acknowledged. This work was also supported by the Strategic Priority Research Program of the Chinese Academy of Sciences (Grant No. XDB22040502), and Collaborative Innovation Center of Suzhou Nano Science and Technology.

References

- 1 J. de Vicente, D. J. Klingenberg and R. Hidalgo-Alvarez, *Soft Matter*, 2011, **7**, 3701–3710.
- 2 H. C. Kim, C. Han, P. Kim and S. B. Choi, *Smart Mater. Struct.*, 2015, **24**, 087002.
- 3 F. Pineux, R. Marega, A. Stopin, A. La Torre, Y. Garcia, E. Devlin, C. Michiels, A. N. Khlobystov and D. Bonifazi, *Nanoscale*, 2015, **7**, 20474–20488.
- 4 A. Aravind, R. Nair, S. Raveendran, S. Veerananarayanan, Y. Nagaoka, T. Fukuda, T. Hasumura, H. Morimoto, Y. Yoshida, T. Maekawa and D. S. Kumar, *J. Magn. Magn. Mater.*, 2013, **344**, 116–123.
- 5 S. S. Sun, J. Yang, W. H. Li, H. X. Deng, H. P. Du and G. Alici, *Smart Mater. Struct.*, 2015, **24**, 085021.
- 6 S. S. Sun, D. H. Ning, J. Yang, H. Du, S. W. Zhang, W. H. Li and M. Nakano, *Smart Mater. Struct.*, 2017, **26**, 085025.
- 7 J. W. Lee, K. P. Hong, M. W. Cho, S. H. Kwon and H. J. Choi, *Smart Mater. Struct.*, 2015, **24**, 065002.
- 8 S. Lee, K. Y. Shin and J. Jang, *Nanoscale*, 2015, **7**, 9646–9654.
- 9 Z. Laherisheth and R. V. Upadhyay, *Smart Mater. Struct.*, 2017, **26**, 054008.
- 10 F. Vereda, J. P. Segovia-Gutierrez, J. de Vicente and R. Hidalgo-Alvarez, *J. Phys. D: Appl. Phys.*, 2015, **48**, 015309.
- 11 R. V. Upadhyay, Z. Laherisheth and K. Shah, *Smart Mater. Struct.*, 2014, **23**, 015002.
- 12 M. T. Lopez-Lopez, P. Kuzhir and G. Bossis, *J. Rheol.*, 2009, **53**, 115–126.
- 13 I. Jonkkari, M. Isakov and S. Syrjala, *J. Intell. Mater. Syst. Struct.*, 2015, **26**, 2256–2265.
- 14 M. Ashtiani, S. H. Hashemabadi and A. Ghaffari, *J. Magn. Magn. Mater.*, 2015, **374**, 716–730.
- 15 M. Cerbelaud, A. Videcoq, L. Alison, E. Tervoort and A. R. Studart, *Langmuir*, 2017, **33**, 14347–14357.
- 16 M. Machovsky, M. Mrlik, I. Kuritka, V. Pavlinek and V. Babayan, *RSC Adv.*, 2014, **4**, 996–1003.
- 17 J. S. An, W. J. Han and H. J. Choi, *Colloids Surf., A*, 2017, **535**, 16–23.
- 18 F. F. Fang, J. H. Kim and H. J. Choi, *Polymer*, 2009, **50**, 2290–2293.
- 19 H. T. Pu and F. J. Jiang, *Nanotechnology*, 2005, **16**, 1486–1489.
- 20 S. H. Xuan, L. Y. Hao and K. C. F. Leung, *New J. Chem.*, 2014, **38**, 6125–6132.
- 21 H. T. Pu, F. J. Jiang and Z. L. Yang, *Mater. Chem. Phys.*, 2006, **100**, 10–14.
- 22 J. S. An, W. J. Han and H. J. Choi, *Colloids Surf., A*, 2017, **535**, 16–23.
- 23 K. Shahrivar, E. Carreon-Gonzalez, J. R. Morillas and J. de Vicente, *Soft Matter*, 2017, **13**, 2677–2685.

- 24 W. H. Li and H. Du, *Int. J. Adv. Des. Manuf. Technol.*, 2003, **21**, 508–515.
- 25 D. A. Bompos and P. G. Nikolakopoulos, *Simul. Model. Pract. Th.*, 2011, **19**, 1035–1060.
- 26 K. Okada and A. Satoh, *J. Magn. Magn. Mater.*, 2017, **437**, 29–41.
- 27 J. A. Ruiz-Lopez, Z. W. Wang, J. C. Fernandez-Toledano, R. Hidalgo-Alvarez and J. de Vicente, *Rheol. Acta*, 2016, **55**, 245–256.
- 28 J. A. Ruiz-Lopez, Z. W. Wang, R. Hidalgo-Alvarez and J. de Vicente, *J. Rheol.*, 2017, **61**, 871–881.
- 29 X. H. Ruan, L. Pei, S. H. Xuan, Q. F. Yan and X. L. Gong, *J. Magn. Magn. Mater.*, 2017, **429**, 1–10.
- 30 B. D. Cullity and C. D. Graham, *Introduction to magnetic materials*, John Wiley & Sons, New York, 2011.
- 31 K. H. Kim, M. J. Kim, Y. H. Choa, D. H. Kim and J. H. Yu, *IEEE Trans. Magn.*, 2008, **44**, 2940–2943.
- 32 D. X. Chen, A. Sanchez, E. Taboada, A. Roig, N. Sun and H. C. Gu, *J. Appl. Phys.*, 2009, **105**, 083924.
- 33 E. E. Keaveny and M. R. Maxey, *J. Comput. Phys.*, 2008, **227**, 9554–9571.
- 34 T. X. Liu, X. L. Gong, Y. G. Xu, S. H. Xuan and W. Q. Jiang, *Soft Matter*, 2013, **9**, 10069–10080.
- 35 V. A. Parsegian, *Van der Waals forces: a handbook for biologists, chemists, engineers, and physicists*, Cambridge University Press, Cambridge, 2005.
- 36 B. Faure, G. Salazar-Alvarez and L. Bergstrom, *Langmuir*, 2011, **27**, 8659–8664.
- 37 D. J. Klingenberg, C. H. Olk, M. A. Golden and J. C. Ulicny, *J. Phys.: Condens. Matter*, 2010, **22**, 324101.
- 38 L. He, D. K. Tafti and K. Nagendra, *Powder Technol.*, 2017, **313**, 332–343.
- 39 E. E. Michaelides, *Int. J. Heat Mass Transfer*, 2015, **81**, 179–187.
- 40 R. D. Groot and P. B. Warren, *J. Chem. Phys.*, 1997, **107**, 4423–4435.
- 41 M. P. Allen and D. J. Tildesley, *Computer simulation of liquids*, Oxford University Press, New York, 2017.
- 42 Y. Tian, J. L. Jiang, Y. G. Meng and S. Z. Wen, *Appl. Phys. Lett.*, 2010, **97**, 151904.
- 43 D. J. Klingenberg, J. C. Ulicny and M. A. Golden, *J. Rheol.*, 2007, **51**, 883–893.
- 44 D. Susan-Resiga and L. Vekas, *J. Rheol.*, 2017, **61**, 401–408.
- 45 S. G. Sherman, A. C. Becnel and N. M. Wereley, *J. Magn. Magn. Mater.*, 2015, **380**, 98–104.